ACS Energy LETTERS

http://pubs.acs.org/journal/aelccp

LETTER

Multisource Vacuum Deposition of Methylammonium-Free Perovskite Solar Cells

Yu-Hsien Chiang, Miguel Anaya, and Samuel D. Stranks*

Cite This: *ACS Energy Lett.* 2020, 5, 2498–2504

Read Online

ACCESS | Metrics & More | Article Recommendations | Supporting Information

ABSTRACT: Halide perovskites of the form ABX_3 have shown outstanding properties for solar cells. The highest reported compositions consist of mixtures of A-site cations methylammonium (MA), formamidinium (FA) and cesium, and X-site iodide and bromide ions, and are produced by solution processing. However, it is unclear whether solution processing will yield sufficient spatial performance uniformity for large-scale photovoltaic modules or compatibility with deposition of multilayered tandem solar cell stacks. In addition, the volatile MA cation presents long-term stability issues. Here, we report the multisource vacuum deposition of $FA_{0.7}Cs_{0.3}Pb(I_{0.9}Br_{0.1})_3$ perovskite thin films with high-quality morphological, structural, and optoelectronic properties. We find that the controlled addition of excess PbI_2 during the deposition is critical for achieving high performance and stability of the absorber material, and we fabricate *p-i-n* solar cells with stabilized power output of 18.2%. We also reveal the sensitivity of the deposition process to a range of parameters, including substrate, annealing temperature, evaporation rates, and source purity, providing a guide for further evaporation efforts. Our results demonstrate the enormous promise for MA-free perovskite solar cells employing industry-scalable multisource evaporation processes.

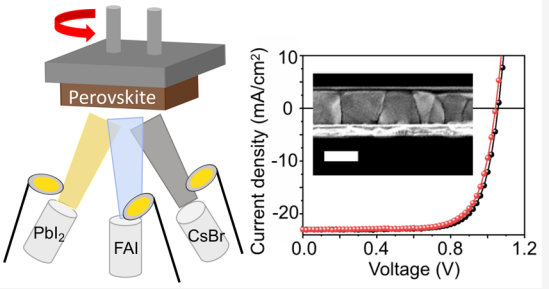

Halide perovskite semiconductors have attracted significant attention because of their excellent optoelectronic properties, which, for solar cells, includes high absorption coefficients, long charge-carrier diffusion lengths, and low exciton binding energies.[1,2] The tunable ABX_3 structure, where A is a cation such as cesium (Cs), methylammonium (MA), and/or formamidinium (FA); B is a divalent metal cation such as lead (Pb) or tin (Sn); and X is a halide (iodide (I), bromide (Br), and/or chloride (Cl)), allows us to tune the optoelectronic properties such as bandgap for different device demands.[3] Perovskite solar cells have surpassed 25% power conversion efficiency (PCE) by solution-processed methods and are approaching performances of market-leading crystalline silicon.[4] The highest performing, most stable, and readily reproducible solution-processed perovskite solar cells employ absorbers comprising mixtures of A-site cations and X-site cations, for example, the triple cation composition $Cs_{0.05}(MA_{0.17}FA_{0.83})_{0.95}Pb(I_{0.83}Br_{0.17})_3$ or the MA-free double-cation analogue.[5,6] However, industrial application requires scaling up the processes with high spatial uniformity and reproducible performance parameters on a number of underlying layer stacks, and it is unclear that solution methods will meet these stringent criteria. In addition, the solutions employed to fabricate perovskite solar cells such as dimethylformamide are toxic, and there are not yet clear alternatives that can match these performances.[7]

Vacuum deposition is a mature technique in the semiconductor industry to fabricate highly uniform and pinhole-free films at a large scale on different types of substrates including planar or textured surfaces.[8−12] Furthermore, vacuum deposition allows strict control over film composition and thickness, which will be critical for achieving sufficient film uniformity at scale.[13] To date, the PCE of perovskite solar cells fabricated by simultaneous multisource deposition is still lagging behind their solution-processed counterparts, in part because of the more limited literature around the vacuum deposition of perovskite films relative to the solution-processed literature, which has a lower equipment entry barrier. There is also a number of nontrivial challenges unique to vapor deposition, including optimizing source evaporation, rates, growth processes, and engineering solutions to prevent source cross-talk of volatile substances, to name a few. The highest PCE of a vacuum-deposited perovskite solar cell is 20.8% based on a $MAPbI_3$ composition, with an encouraging 18.2% for a 20 cm^2 device.[14,15] However, the volatile character of the

Received: April 17, 2020
Accepted: June 25, 2020
Published: June 25, 2020

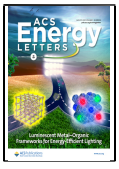

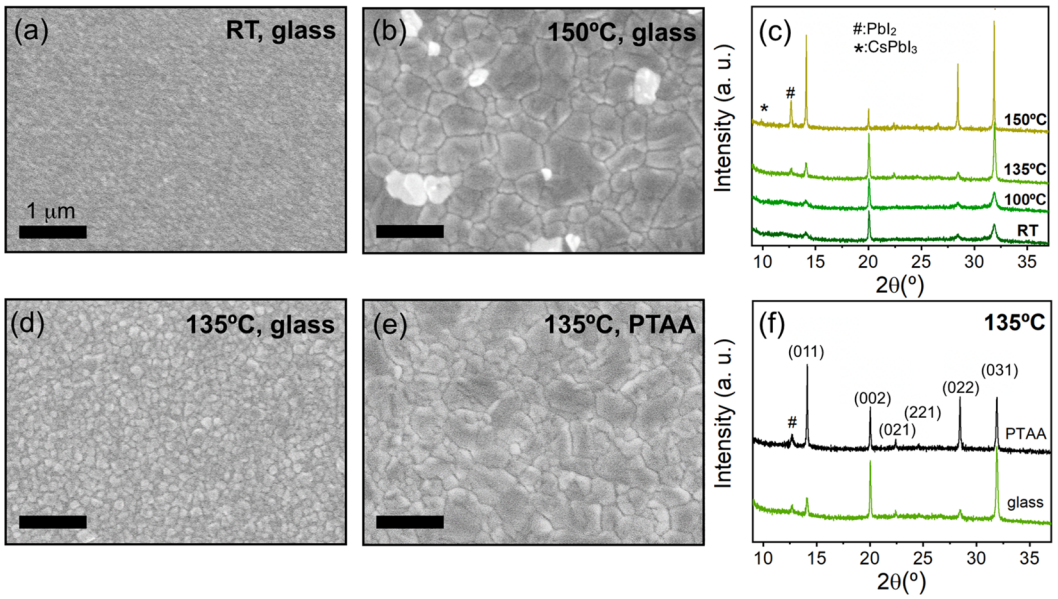

Figure 1. SEM top view images showing the morphology of evaporated $FA_{0.7}Cs_{0.3}Pb(I_{0.9}Br_{0.1})_3$ perovskite films on glass as-deposited (a) and after 30 min of annealing at 150 °C (b). (c) Room-temperature XRD patterns corresponding to evaporated perovskite films on glass following annealing at different temperatures for 30 min. Peaks corresponding to additional PbI_2 and $CsPbI_3$ phases are labeled; the other peaks correspond to the alloyed perovskite. SEM top view images displaying the morphology differences when the perovskite films are evaporated on glass (d) and PTAA (e) and annealed at an optimum temperature of 135 °C; their corresponding XRD patterns (f). The perovskite XRD peaks are assigned based on Pawley refinements (Figure S4). XRD patterns are vertically offset for clarity.

MA cation hampers the stability of the device, especially at temperatures above 80 °C, presenting hurdles for such cells to pass all critical photovoltaic stress tests to validate long-term stability.[16−18] Therefore, evaporation of MA-free perovskite compositions represents a promising new direction albeit a significant challenge for the field. Borchert et al. reported evaporated $FAPbI_3$-based *n-i-p* solar cells with PCE of 15.8% and stabilized power output (SPO) of 14.2%.[19] However, pure $FAPbI_3$ perovskite will compromise operational stability as the black-phase readily converts to a yellow δ-phase at room temperature because of the large FA cation distorting the cubic structure.[20] In order to stabilize the black perovskite phase, Gil-Escrig et al. proposed a mixed cation and mixed halide $FA_{0.5}Cs_{0.5}Pb(I_{0.83}Br_{0.17})_3$ composition to achieve a PCE of 9.6%, though there was still δ-phase $FAPbI_3$ observed in the film.[10] As a result, the addition of MA was required to suppress the formation of the unwanted yellow δ-phase, leading to better perovskite films and a higher PCE of 16%. There remains a challenge to vacuum deposit MA-free mixed cation, mixed halide perovskite films to achieve the required combination of both film stability and solar cell performance that could ultimately rival the parameters of their solution-processed counterparts.

In this work, we develop a three-source thermal evaporation vacuum deposition protocol simultaneously using FAI, PbI_2, and CsBr sources to attain high-quality and highly reproducible $FA_{0.7}Cs_{0.3}Pb(I_{0.9}Br_{0.1})_3$ thin films. We identify that the resulting film quality is highly sensitive to a number of experimental parameters, including substrate surface, source purities, relative evaporation rates between the sources, and annealing temperature, highlighting critical parameters that need global consideration for further device developments. We found that the optimal film structure and morphology was attained by inclusion of a small excess of PbI_2, which also led to higher photoluminescence quantum efficiencies (PLQEs) and longer charge carrier lifetimes. We fabricate *p-i-n* solar cells with a planar architecture, achieving an SPO of 18.2%, which is to date the highest performance for a vacuum-deposited MA-free based perovskite. Such cells, deposited on *p-i-n* architectures and fabricated at low temperature, are compatible with more complicated multilayer tandem stacks and flexible, lightweight substrates.

We simultaneously evaporated FAI, CsBr, and PbI_2 to form mixed-cation lead mixed-halide perovskite films (see the Supporting Information for detailed methods). For any given deposition, the source rates were fixed by allowing the respective source temperatures to vary (see Figure S1). We used a profilometer to calibrate the tooling factors of the individual precursors and final perovskite film to confirm film uniformity across 10 × 10 cm^2 (see Table S1 for deposition parameters such as tooling factor, Z-factor, and substrate rotation speed, and Methods for further details). The final perovskite film thickness was set to typical solar cell device absorber layer values (∼500 nm). We modified the nominal film composition by changing the relative ratios of the rates for each source for a given deposition run, converging on a combination of rates that give a nominal stoichiometric composition corresponding approximately to $FA_{0.7}Cs_{0.3}Pb(I_{0.9}Br_{0.1})_3$ (see Figures S2 and S3 for details). We note that we needed to evaporate an excess of FAI to achieve a stoichiometric composition, which we attribute to issues with the organic component adhering to the substrate.[21,22]

Scanning electron microscopy (SEM) images reveal that morphological grains in as-deposited films on UV-ozone-treated glass are ∼50 nm in size (Figure 1a), but after the deposited films are annealed at 150 °C for 30 min, larger entities of up to 1−2 μm form (Figure 1b), consistent with the sharpening of the XRD peaks upon annealing (Figure 1c). We show in Figure 1c the progression of the room-temperature XRD profiles as the postdeposition annealing temperature is

https://dx.doi.org/10.1021/acsenergylett.0c00839
ACS Energy Lett. 2020, 5, 2498−2504

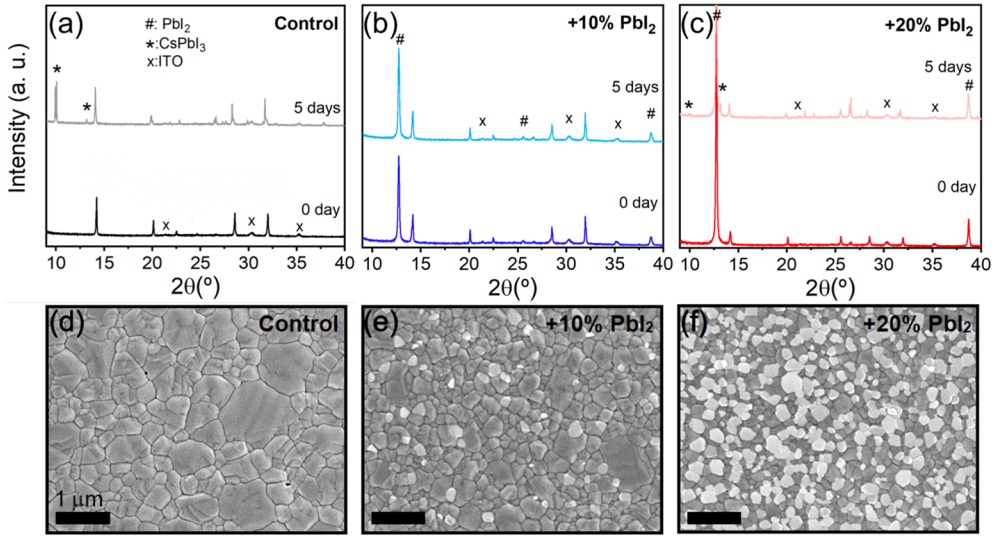

Figure 2. Morphological and structural characterization of evaporated and annealed $FA_{0.7}Cs_{0.3}Pb(I_{0.9}Br_{0.1})_3$ perovskite thin films on ITO/PTAA substrates with different fractions of excess PbI_2. (a–c) XRD diffraction patterns as prepared (and annealed) and after storage in air at 50% relative humidity for 5 days. XRD patterns are vertically offset for clarity. We assign the peaks at ∼10° and 13.1° to $CsPbI_3$, although we note that this phase could also contain fractions of bromide. (d–f) SEM micrographs of the films.

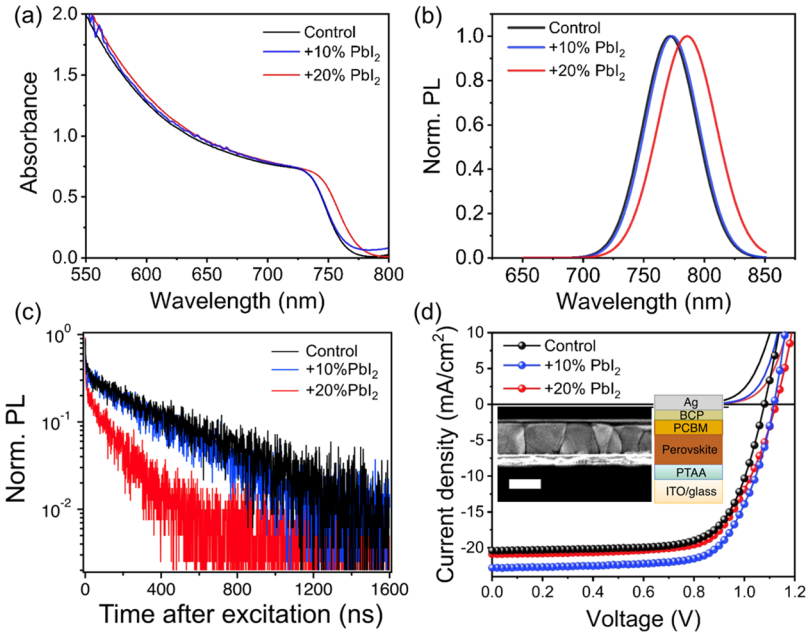

Figure 3. UV–Vis absorption (a) and normalized photoluminescence (PL) (b) spectra (excitation at 520 nm) of evaporated $FA_{0.7}Cs_{0.3}Pb(I_{0.9}Br_{0.1})_3$ perovskite films with different quantities of excess PbI_2 with respect to the stoichiometric control sample. (c) TRPL measurements for the different perovskite films with excitation at 407 nm (repetition rate of 0.5 MHz, fluence of 5 nJ/cm^2/pulse). (d) J–V curves of evaporated perovskite solar cells with different quantities of excess PbI_2 measured under AM 1.5G (100 mW/cm^2 irradiance), along with corresponding dark curves. The curves are from the reverse scan (sweeping from 1.2 V to −0.1 V). A cross-sectional SEM image (scale bar is 500 nm) and a schematic of the employed solar cell architecture are shown in the inset.

changed, revealing an increase in the peak at 2θ = 14.15° corresponding to the black absorbing perovskite phase identified as the (011) peak (Figure S4; see labels on Figure 1f). Although the perovskite film annealed at 150 °C exhibits the largest grain sizes and highest perovskite-peak crystallinity, there is a new $CsPbI_3$ peak at ∼10°, indicating the presence of an unwanted additional phase. Therefore, we identified 135 °C as the optimum annealing temperature.

We also observe that the perovskite film properties are particularly sensitive to the underlying substrate, likely because of different surface chemistry in each case. We find that the perovskite grain size when deposited on the bottom *p*-type solar cell contact poly(triarylamine) (PTAA, Figure 1e) is significantly larger than that of the film deposited on glass (Figure 1d). Likewise, the perovskite crystallinity and structure orientation also vary with the substrate, with the perovskite deposited on PTAA showing stronger black perovskite phase-related reflections than when the material is evaporated on glass (Figure 1f). Thus, to ensure we optimize the material growth on the specific substrate relevant to our devices, we

https://dx.doi.org/10.1021/acsenergylett.0c00839
ACS Energy Lett. 2020, 5, 2498–2504

herein performed depositions on PTAA substrates with an underlying indium tin oxide (ITO) layer and an annealing temperature of 135 °C, unless stated otherwise.

To test the atmospheric stability of the stoichiometric films, we stored them in ambient air with a relative humidity of 50 ± 5% for a period of 5 days and assessed changes in the XRD patterns (Figure 2a). We found that the samples stored in air showed substantial phase segregation over time under exposure, with the appearance of two new peaks at 2θ = 10° and 13.1° that we assign to the orthorhombic $CsPbI_3$ yellow-phase.[23−25] We identify moisture as the primary cause of this degradation because the perovskite quality is preserved when we store the samples in dry air (relative humidity <10%); protection of the films with standard contact layers did not mitigate the degradation process in the presence of moisture (Figure S5).

We now varied the PbI_2 precursor evaporation rate to finely tune its content in the final film to be +10% and +20% with respect to the stoichiometric control sample. The addition of PbI_2 results in strong XRD peaks at 2θ = 12.7° (corresponding to crystalline PbI_2), concomitant with a slight decrease in the perovskite (011) peak (2θ = 14.14° and 14.12°) for both the +10% (Figure 2b) and +20% (Figure 2c) samples (see Figure S6 for a zoomed-in view of the XRD data). Nevertheless, we found that the stability under ambient conditions was remarkably increased for the films with excess PbI_2, with no detectable phase segregation observed after 5 days for the +10% PbI_2 sample and only a small amount of orthorhombic $CsPbI_3$ signal noticeable after 32 days in humid air (Figure S7). We also find that the films with excess PbI_2 do not show degradation even after 8 h of heating at 135 °C inside a nitrogen-filled glovebox (Figures S8 and S9), which we attribute to the MA-free nature of the system.[17] SEM images show that the addition of PbI_2 causes a decrease and homogenization in the size of the perovskite grains from an average size of ∼335 nm for the control (Figure 2d) to ∼209 nm for +10% (Figure 2e) (see Figure S10 for the grain size distributions); these results are in line with the slight broadening in the perovskite peaks in the XRD patterns (cf. Figure 2a−c). Moreover, we find that the excess PbI_2 forms as clusters as revealed by bright areas in the micrographs, which are particularly evident in the +20% sample (Figure 2f).[26] We propose that the excess PbI_2 particularly situated at the grain boundaries could form a protection layer against moisture infiltration.[27] We also note that our optimal parameters change when using a different PbI_2 supplier, further emphasizing the sensitivity of the process (Figure S11).

To assess the resulting optoelectronic properties of the films, we show absorbance spectra in Figure 3a, revealing an absorption onset at ∼765 nm for the control film which red-shifts to ∼767 and ∼775 nm with 10% and 20% PbI_2 excess, respectively. We find a similar trend in the PL peaks, which also red-shift by ∼2 and ∼10 nm with addition of 10% and 20% excess PbI_2, respectively (Figure 3b). We associate these reduced absorption onset and emission energies to a higher fraction of I/(I + Br) in the perovskite structure (i.e., dilution of Br), which is consistent with the shift of the perovskite peak toward lower angle in XRD (Figure S6). We also find that the PLQE of the films on glass under approximately 1 sun equivalent excitation density (520 nm CW laser at 60 mW/cm^2) is enhanced in the samples with 10% and 20% excess PbI_2, with PLQE values of 0.5% and 0.3%, respectively, compared to 0.2% measured for the control sample (see also Figure S12). We attribute this observation to the passivating nature of PbI_2 in the perovskite films.[28,29] This passivation of defects may also be related to the improved air stability of perovskite films with 10% PbI_2 incorporation, in line with proposed links between nonradiative centers and sites of instability (such as ion migration and environmental susceptibility).[30,31] Further, time-resolved PL measurements under fluences similar to 1 sun illumination reveal an initial fast component but long lifetime components for the control, 10%, and 20% perovskite films of 401, 204, and 130 ns, respectively, where lifetime is defined as the time taken to fall to 1/e of the initial intensity of the long decay component (Figure 3c). These values are an order of magnitude longer than the values of a few nanoseconds reported for most evaporated perovskite films in the literature to date.[19,32] We note there is an initial fast decay component in all of our samples that is likely due to nonradiative recombination and is consistent with the PLQE values being significantly less than unity; it is likely that further surface passivation work will reduce these losses further.

We fabricated solar cell devices with an inverted architecture: ITO/PTAA/evaporated perovskite/phenyl-C61-butyric acid methyl ester (PCBM)/bathocuproine (BCP)/silver (Ag) and encapsulated them with a glass cover slide in a nitrogen-filled glovebox. We display in Figure 3d a schematic of the device architecture along with a cross-sectional SEM image, which shows a perovskite film with a thickness of ∼490 nm with large, homogeneous morphological grains. We compare the performance of devices under AM 1.5 G illumination with different amounts of PbI_2 additives in Table 1 and show the corresponding current−voltage (J−V) curves in Figure 3d. For the stoichiometric perovskite composition (no excess PbI_2), the device presents a PCE of 15.5%, an open-circuit voltage (V_{oc}) of 1.08 V, a short-circuit current density (J_{sc}) of 20.4 mA/cm^2, and a fill factor (FF) of 70.4%. With the addition of 10% excess PbI_2, both V_{oc} and J_{sc} are increased to 1.12 V and 22.8 mA/cm^2, respectively, yielding a PCE of 17.8%. We note that the measured voltage of 1.12 V matches the value expected from PLQE measurements of the full device stack under solar illumination conditions (0.05%, Figure S13). For 20% excess PbI_2, the device performance drops to 16.1% with lower J_{sc} and FF, likely because of the excess PbI_2 starting to hinder charge transport and/or collection (cf. Figure 2f). In general, with more PbI_2 the device open-circuit voltage increases, which is in line with the increased luminescence efficiency and passivation effect. We also observe that hysteresis between the forward and reverse scans is low in each of the devices (Figure S14), though the hysteresis significantly increases if the PbI_2 deposition rate is unstable in a given batch (Figure S15). This observation is also reflected in far less homogeneous films when the rate is unstable, with clear phase segregation in the case of unstable

Table 1. Device Performance Parameters from the Reverse Scans of the $FA_{0.7}Cs_{0.3}Pb(I_{0.9}Br_{0.1})_3$ Solar Cells with Different Amounts of Excess PbI_2 with Respect to the Control

	V_{OC} (V)	J_{SC} (mA/cm^2)	FF (%)	PCE (%)
control	1.08	−20.4	70.4	15.5
5%	1.06	−23.0	74.6	18.1
10%	1.12	−22.8	70.1	17.8
20%	1.12	−20.9	68.7	16.1

https://dx.doi.org/10.1021/acsenergylett.0c00839
ACS Energy Lett. 2020, 5, 2498−2504

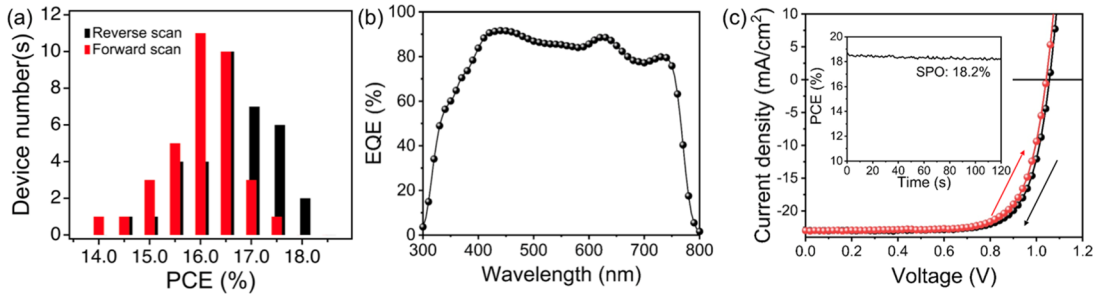

Figure 4. (a) Histogram of device performances from 35 independent devices with the $FA_{0.7}Cs_{0.3}Pb(I_{0.9}Br_{0.1})_3$ perovskite including 5% excess PbI_2. The results from reverse (1.2 V to −0.1 V, black curve) and forward (−0.1 to 1.2 V, red curve) scans are distinguished. (b) EQE measurement for the champion device. (c) Forward (red) and reverse (black) *J*−*V* curves of a champion device. The inset figure is the stabilized power output (SPO) measurement, maintaining the bias at maximum power point of the reverse scan at 0.88 V and measuring the photocurrent.

rates (Figures S16 and S17). These results emphasize the importance of the composition, achieved through precisely controlled deposition rates, to yield high-quality perovskite films and devices by vapor deposition.

Finally, we further optimize the PbI_2 excess and find that our best-performing solar cells are based on a perovskite composition with 5% excess PbI_2 (Table 1). This composition results in a small fraction of crystalline PbI_2 in the final films that provides a compromised balance of passivation and stabilization of the films without hindering current collection (related to current density) or increasing series resistance (related to fill factor); the PbI_2 entities in these films are too small to be resolved in SEM images (see Figure S18 for film characterization). We show the device performance statistics in Figure 4a with forward (from short circuit to open circuit) and reverse scan (from open circuit to short circuit) results from 35 independent devices across five different batches. We note that the batch-to-batch variation is low (see Figure S19). The device metrics are highly reproducible with an average PCE for reverse and forward scans of 16.8 ± 0.8% and 16.2 ± 0.9%, respectively. We observed no degradation in performance of an encapsulated device over a period of 18 days stored in air (Figure S20), reflecting the film stability observed in Figure 2 in samples with excess PbI_2. We display the external quantum efficiency (EQE) of our champion device in Figure 4b, with values greater than 80% for the working spectral range 400−775 nm, demonstrating an excellent photon-to-electron conversion efficiency. Interestingly, the spectrum shows oscillating features that are fingerprints of light interference phenomena arising from the high optical quality of the device stack. The SPO of the champion device reaches 18.2% with negligible hysteresis effect between the forward and backward curves (Figure 4c). This result represents the best performing MA-free perovskite solar cell by vacuum deposition to date. Finally, a proof of principle stability test shows that the champion device composition retains ∼90% of its initial efficiency after 35 h under continuous operation at maximum power point (Figure S21), which is an extremely encouraging result for vacuum-deposited MA-free perovskite solar cells given the device stack has not been optimized for stability.

In conclusion, we simultaneously use three thermal sources to evaporate MA-free perovskite films with $FA_{0.7}Cs_{0.3}Pb(I_{0.9}Br_{0.1})_3$ composition. We found that an excess of PbI_2 from the nominal stoichiometric composition enhances the film stability and optoelectronic properties, yielding a greater PLQE and long charge carrier lifetimes. We demonstrate solar cells with a *p-i-n* architecture showing stabilized power output of 18.2%, which is the highest performance for a vapor-deposited MA-free system. We highlight the extreme sensitivity of the resulting film and device properties to a range of processing conditions, including precursor rates and rate stability, precursor supplier, postannealing temperature, and underlying substrates, providing clear guidelines for further optimization and deposition of different compositions. These results provide a major step toward MA- and solvent-free, scalable, and reproducible methodologies suitable for the adoption of perovskite technology in production chains and applications such as multijunction devices where solution methods are less preferred.

■ ASSOCIATED CONTENT

Supporting Information

The Supporting Information is available free of charge at https://pubs.acs.org/doi/10.1021/acsenergylett.0c00839.

Materials and methods, deposition rates and temperatures, XRD data of solution-processed samples, Pawley fitting, SEM results, thermal stability data, XRD of degraded and rate-dependent films, PL and hyperspectral PL measurements, *J*−*V* curves, and device stability (PDF)

■ AUTHOR INFORMATION

Corresponding Author

Samuel D. Stranks − *Cavendish Laboratory and Department of Chemical Engineering & Biotechnology, University of Cambridge, Cambridge CB3 0HE, United Kingdom;* orcid.org/0000-0002-8303-7292; Email: sds65@cam.ac.uk

Authors

Yu-Hsien Chiang − *Cavendish Laboratory, University of Cambridge, Cambridge CB3 0HE, United Kingdom*

Miguel Anaya − *Cavendish Laboratory, University of Cambridge, Cambridge CB3 0HE, United Kingdom;* orcid.org/0000-0002-0384-5338

Complete contact information is available at: https://pubs.acs.org/10.1021/acsenergylett.0c00839

Notes

The authors declare the following competing financial interest(s): Samuel D. Stranks is a Co-Founder of Swift Solar Inc.

https://dx.doi.org/10.1021/acsenergylett.0c00839
ACS Energy Lett. 2020, 5, 2498−2504

■ ACKNOWLEDGMENTS

S.D.S. and M.A. acknowledge funding from the European Research Council (ERC) (Grant Agreement No. 756962 [HYPERION]) and the Marie Skłodowska-Curie actions (Grant Agreement No. 841386) under the European Union's Horizon 2020 research and innovation programme. S.D.S acknowledges support from the Royal Society and Tata Group (UF150033). Y.-H.C. acknowledges funding from a Taiwan Cambridge Scholarship. Part of this work was undertaken using equipment facilities provided by the Henry Royce Institute, via the grant Henry Royce Institute, Cambridge Equipment: EP/P024947/1. The authors acknowledge the Engineering and Physical Research Council (EPSRC) (EP/R023980/1) and the EPSRC "Centre for Advanced Materials for Integrated Energy Systems (CAM-IES)" (EP/P007767/1) for funding. We thank Tiarnan Doherty and Tim van de Goor for useful discussions.

■ REFERENCES

(1) Green, M. A.; Ho-Baillie, A.; Snaith, H. J. The Emergence of Perovskite Solar Cells. *Nat. Photonics* **2014**, *8*, 506−514.

(2) Stranks, S. D.; Eperon, G. E.; Grancini, G.; Menelaou, C.; Alcocer, M. J. P.; Leijtens, T.; Herz, L. M.; Petrozza, A.; Snaith, H. J. Electron-Hole Diffusion Lengths Exceeding 1 Micrometer in an Organometal Trihalide Perovskite Absorber. *Science* **2013**, *342*, 341−344.

(3) Noh, J. H.; Im, S. H.; Heo, J. H.; Mandal, T. N.; Seok, S. I. Chemical Management for Colorful, Efficient, and Stable Inorganic−Organic Hybrid Nanostructured Solar Cells. *Nano Lett.* **2013**, *13*, 1764−1769.

(4) NREL chart. https://www.nrel.gov/pv/assets/pdfs/best-research-cell-efficiencies.20200218.pdf (accessed 2020-02-25).

(5) Saliba, M.; Matsui, T.; Seo, J.-Y.; Domanski, K.; Correa-Baena, J.-P.; Nazeeruddin, M. K.; Zakeeruddin, S. M.; Tress, W.; Abate, A.; Hagfeldt, A.; et al. Cesium-Containing Triple Cation Perovskite Solar Cells: Improved Stability, Reproducibility and High Efficiency. *Energy Environ. Sci.* **2016**, *9*, 1989−1997.

(6) Min, H.; Kim, M.; Lee, S.-U.; Kim, H.; Kim, G.; Choi, K.; Lee, J. H.; Seok, S. I. Efficient, Stable Solar Cells by Using Inherent Bandgap of α-Phase Formamidinium Lead Iodide. *Science* **2019**, *366*, 749−753.

(7) Noel, N. K.; Habisreutinger, S. N.; Wenger, B.; Klug, M. T.; Hörantner, M. T.; Johnston, M. B.; Nicholas, R. J.; Moore, D. T.; Snaith, H. J. A Low Viscosity, Low Boiling Point, Clean Solvent System for the Rapid Crystallisation of Highly Specular Perovskite Films. *Energy Environ. Sci.* **2017**, *10*, 145−152.

(8) Liu, M.; Johnston, M. B.; Snaith, H. J. Efficient Planar Heterojunction Perovskite Solar Cells by Vapour Deposition. *Nature* **2013**, *501*, 395−398.

(9) Sahli, F.; Werner, J.; Kamino, B. A.; Bräuninger, M.; Monnard, R.; Paviet-Salomon, B.; Barraud, L.; Ding, L.; Diaz Leon, J. J.; Sacchetto, D.; et al. Fully Textured Monolithic Perovskite/Silicon Tandem Solar Cells with 25.2% Power Conversion Efficiency. *Nat. Mater.* **2018**, *17*, 820−826.

(10) Gil-Escrig, L.; Momblona, C.; La-Placa, M.-G.; Boix, P. P.; Sessolo, M.; Bolink, H. J. Vacuum Deposited Triple-Cation Mixed-Halide Perovskite Solar Cells. *Adv. Energy Mater.* **2018**, *8*, 1703506.

(11) Kazmerski, L. L.; White, F. R.; Ayyagari, M. S.; Juang, Y. J.; Patterson, R. P. Growth and Characterization of Thin-film Compound Semiconductor Photovoltaic Heterojunctions. *J. Vac. Sci. Technol.* **1977**, *14*, 65−68.

(12) Holloway, H.; Richards, J. L.; Bobb, L. C.; Perry, J.; Zimmerman, E. Oriented Growth of Semiconductors. IV. Vacuum Deposition of Epitaxial Indium Antimonide. *J. Appl. Phys.* **1966**, *37*, 4694−4699.

(13) Swartwout, R.; Hoerantner, M. T.; Bulović, V. Scalable Deposition Methods for Large-Area Production of Perovskite Thin Films. *Energy Environ. Sci.* **2019**, *2*, 119−145.

(14) Pérez-del-Rey, D.; Boix, P. P.; Sessolo, M.; Hadipour, A.; Bolink, H. J. Interfacial Modification for High-Efficiency Vapor-Phase-Deposited Perovskite Solar Cells Based on a Metal Oxide Buffer Layer. *J. Phys. Chem. Lett.* **2018**, *9*, 1041−1046.

(15) Li, J.; Wang, H.; Chin, X. Y.; Dewi, H. A.; Vergeer, K.; Goh, T. W.; Lim, J. W. M.; Lew, J. H.; Loh, K. P.; Soci, C.; Sum, T. C.; Bolink, B. J.; Mathews, N.; Mhaisalkar, S.; Bruno, A. Highly Efficient Thermally Co-evaporated Perovskite Solar Cells and Mini-modules. *Joule* **2020**, *4*, 1035.

(16) Juarez-Perez, E. J.; Hawash, Z.; Raga, S. R.; Ono, L. K.; Qi, Y. Thermal Degradation of $CH_3NH_3PbI_3$ Perovskite into NH_3 and CH_3I Gases Observed by Coupled Thermogravimetry−Mass Spectrometry Analysis. *Energy Environ. Sci.* **2016**, *9*, 3406−3410.

(17) Turren-Cruz, S.-H.; Hagfeldt, A.; Saliba, M. Methylammonium-Free, High-Performance, and Stable Perovskite Solar Cells on a Planar Architecture. *Science* **2018**, *362*, 449.

(18) Khenkin, M. V.; Katz, E. A.; Abate, A.; Bardizza, G.; Berry, J. J.; Brabec, C.; Brunetti, F.; Bulović, V.; Burlingame, Q.; Di Carlo, A.; et al. Consensus Statement for Stability Assessment and Reporting for Perovskite Photovoltaics Based on ISOS Procedures. *Nat. Energy* **2020**, *5*, 35−49.

(19) Borchert, J.; Milot, R. L.; Patel, J. B.; Davies, C. L.; Wright, A. D.; Martínez Maestro, L.; Snaith, H. J.; Herz, L. M.; Johnston, M. B. Large-Area, Highly Uniform Evaporated Formamidinium Lead Triiodide Thin Films for Solar Cells. *ACS Energy Lett.* **2017**, *2*, 2799−2804.

(20) Zheng, X.; Wu, C.; Jha, S. K.; Li, Z.; Zhu, K.; Priya, S. Improved Phase Stability of Formamidinium Lead Triiodide Perovskite by Strain Relaxation. *ACS Energy Lett.* **2016**, *1*, 1014−1020.

(21) Lohmann, K. B.; Patel, J. B.; Rothmann, M. U.; Xia, C. Q.; Oliver, D. J.; Herz, L. M.; Snaith, H. J.; Johnston, M. B. Control over Crystal Size in Vapor Deposited Metal-Halide Perovskite Films. *ACS Energy Lett.* **2020**, *5*, 710−717.

(22) Bækbo, M. J.; Hansen, O.; Chorkendorff, I.; Vesborg, P. C. K. Deposition of methylammonium iodide via evaporation − combined kinetic and mass spectrometric study. *RSC Adv.* **2018**, *8*, 29899−29908.

(23) Marronnier, A.; Roma, G.; Boyer-Richard, S.; Pedesseau, L.; Jancu, J.-M.; Bonnassieux, Y.; Katan, C.; Stoumpos, C. C.; Kanatzidis, M. G.; Even, J. Anharmonicity and Disorder in the Black Phases of Cesium Lead Iodide Used for Stable Inorganic Perovskite Solar Cells. *ACS Nano* **2018**, *12*, 3477−3486.

(24) Sutton, R. J.; Filip, M. R.; Haghighirad, A. A.; Sakai, N.; Wenger, B.; Giustino, F.; Snaith, H. J. Cubic or Orthorhombic? Revealing the Crystal Structure of Metastable Black-Phase $CsPbI_3$ by Theory and Experiment. *ACS Energy Lett.* **2018**, *3*, 1787−1794.

(25) Becker, P.; Márquez, A.; Just, J.; Al-Ashouri, A.; Hages, C.; Hempel, H.; Jošt, M.; Albrecht, S.; Frahm, R.; Unold, T. Low Temperature Synthesis of Stable γ-$CsPbI_3$ Perovskite Layers for Solar Cells Obtained by High Throughput Experimentation. *Adv. Energy Mater.* **2019**, *9*, 1900555.

(26) Luo, D.; Yang, W.; Wang, Z.; Sadhanala, A.; Hu, Q.; Su, R.; Shivanna, R.; Trindade, G. F.; Watts, J. F.; Xu, Z.; et al. Enhanced Photovoltage for Inverted Planar Heterojunction Perovskite Solar Cells. *Science* **2018**, *360*, 1442−1446.

(27) Petrus, M. L.; Hu, Y.; Moia, D.; Calado, P.; Leguy, A. M. A.; Barnes, P. R. F.; Docampo, P. The Influence of Water Vapor on the Stability and Processing of Hybrid Perovskite Solar Cells Made from Non-Stoichiometric Precursor Mixtures. *ChemSusChem* **2016**, *9*, 2699−2707.

(28) Jacobsson, T. J.; Correa-Baena, J.-P.; Halvani Anaraki, E.; Philippe, B.; Stranks, S. D.; Bouduban, M. E. F.; Tress, W.; Schenk, K.; Teuscher, J.; Moser, J.-E.; et al. Unreacted PbI_2 as a Double-Edged Sword for Enhancing the Performance of Perovskite Solar Cells. *J. Am. Chem. Soc.* **2016**, *138*, 10331−10343.

(29) Park, B.; Kedem, N.; Kulbak, M.; Lee, D. Y.; Yang, W. S.; Jeon, N. J.; Seo, J.; Kim, G.; Kim, K. J.; Shin, T. J.; et al. Understanding How Excess Lead Iodide Precursor Improves Halide Perovskite Solar Cell Performance. *Nat. Commun.* **2018**, *9*, 3301.

https://dx.doi.org/10.1021/acsenergylett.0c00839
ACS Energy Lett. 2020, 5, 2498−2504

(30) Stranks, S. D. Nonradiative Losses in Metal Halide Perovskites. *ACS Energy Lett.* **2017**, *2*, 1515−1525.
(31) Wang, R.; Mujahid, M.; Duan, Y.; Wang, Z.-K.; Xue, J.; Yang, Y. A Review of Perovskites Solar Cell Stability. *Adv. Funct. Mater.* **2019**, *29*, 1808843.
(32) Chirvony, V. S.; Sekerbayev, K. S.; Pérez-del-Rey, D.; Martínez-Pastor, J. P.; Palazon, F.; Boix, P. P.; Taurbayev, T. I.; Sessolo, M.; Bolink, H. J. Short Photoluminescence Lifetimes in Vacuum-Deposited $CH_3NH_3PbI_3$ Perovskite Thin Films as a Result of Fast Diffusion of Photogenerated Charge Carriers. *J. Phys. Chem. Lett.* **2019**, *10*, 5167−5172.

https://dx.doi.org/10.1021/acsenergylett.0c00839
ACS Energy Lett. 2020, 5, 2498−2504